Thierry M. Faure
e-mail: thierry.faure@limsi.fr

François Lusseyran
e-mail: francois.lusseyran@limsi.fr

Pierre Gougat
e-mail: gougat@limsi.fr

Laboratoire d'Informatique pour la Mécanique et les Sciences de l'Ingénieur, Unité Propre de Recherche 3251, Centre National de la Recherche Scientifique, Université Pierre et Marie Curie, Paris 6, B.P. 133, 91403 Orsay Cedex, France

François Launay
Institut de Physique Nucléaire d'Orsay, Unité Mixte de Recherche 8608, Centre National de la Recherche Scientifique, 15 rue Georges Clémenceau, 91406 Orsay Cedex, France
e-mail: launayf@ipno.in2p3.fr

Experimental Investigation of the Flow Distribution Inside a Tubular Heat Exchanger

The velocity field inside a new concept of heat exchanger, which is a component of a high protons linear accelerator, is investigated experimentally in order to validate the design. A full scale facility with optical accesses is used for the measurements by particle image velocimetry. The choice of the technique is set by the three-dimensional and strongly unsteady structure of the flow. A filtering procedure is applied to the recorded images before processing the velocity field with an optical flow algorithm using dynamical programming. The distribution of the velocity between the different tubes of the heat exchanger shows a large scatter of flow rate between these tubes. In addition, the turbulence characteristics are presented. [DOI: 10.1115/1.2353277]

1 Introduction

Although a flow developing inside a rectilinear duct is well known, the understanding of the behavior of fluid motion inside a system of branching tubes is difficult. One can argue that linear and singular head losses are tabulated [1], but they are not applicable to complex tube branching and cannot give a precise description of the velocity field. However, such geometries are of interest in many applications, but there is a lack of information about them. Investigations have been conducted for Y-shape bifurcations, such as the lung bifurcations flows. This geometry is characterized by a network of repeatedly bifurcating tubes with a diameter decreasing progressively, each bifurcation is forming an angle of around 70 deg between the two downstream tubes. The Reynolds number is less than and of the order of 10,000. The first experiments were conducted with intrusive techniques, such as pressure probes and hot-wire anemometry [2,3]. Fractal-like branching channel networks were analyzed numerically with temperature effect [4]. The lung bifurcations flows are oscillatory flows, and visualizations have been carried out [5]. The issue of drops dynamics inside the lung geometry has been studied numerically using a boundary integral formulation [6]. Recent numerical simulations have also been done for a better understanding of the flow structure and particle deposits [7,8]. Extensive investigations have been conducted with laser Doppler velocimetry (LDV) and particle image velocimetry (PIV) oscillatory flows [9–12]. Another type of Y-shape bifurcation flow is the blood flow in arteries, with geometry close to that of the lung bifurcation [13]. Doppler ultrasonic velocimetry measurements and visualizations have been conducted inside the Y-shape bifurcation of a rectangular section channel with different bifurcation angles [14]. A variation of the Y-shape bifurcation is the 45 deg junction investigated for laminar inlet conditions [15]. An industrial domain of application of branching tube flows is flat plate solar energy collectors [16]. In that geometry, there is a straight-angle bifurcation, and the change in diameter between the upstream and downstream tubes generates strong singularities and recirculation regions. PIV measurements have been conducted in a 90 deg bifurcation under pulsating conditions, within a rectangular section channel [17].

The present work reports the measured flow inside a new heat exchanger design, which is a component of a high-current protons linear accelerator, for inlet flow rates in the operating range 3–15 l/min. The objective is to provide a complete set of data for understanding the fluid dynamics inside the exchanger and for future comparison to numerical simulations for a validation of the design. Its geometry is three-dimensional and combines bifurcations with an angle of 70 deg and orthogonal branching of six tubes with a change of diameter. This geometry is original, and the turbulence characteristics are helpful for understanding heat transfer. Particular attention is devoted to the comparison of the measured velocity distribution between each of the six tubes because the flow rate distribution inside the tubes is the main technological issue.

2 Experimental Setup

2.1 Hydraulic Loop. The hydraulic loop is made of a water circuit to feed the heat exchanger model (Fig. 1). A single stage radial pump rotating at a nominal speed of 2850 rpm permits the water circulation inside the closed-loop circuit. It is fed by a 30 l water tank with a bypass on the pump outlet. Downstream of the pump, there is a regulation valve and two flowmeters for the measurement of the inlet flow rate. The water goes through the heat exchanger model and comes back toward the feeding tank. Flow seeding is provided by 10 μm dia glass spheres coated with a silver film; their density is 1400 kg/m^3.

2.2 Heat Exchanger Model. The new concept of the heat exchanger for cooling the high-current protons accelerator is given in Fig. 2. It depicts a complex three-dimensional geometry

Contributed by the Fluids Engineering Division of ASME for publication in the JOURNAL OF FLUIDS ENGINEERING. Manuscript received July 7, 2005; final manuscript received May 15, 2006. Assoc. Editor: Malcolm J. Andrews.

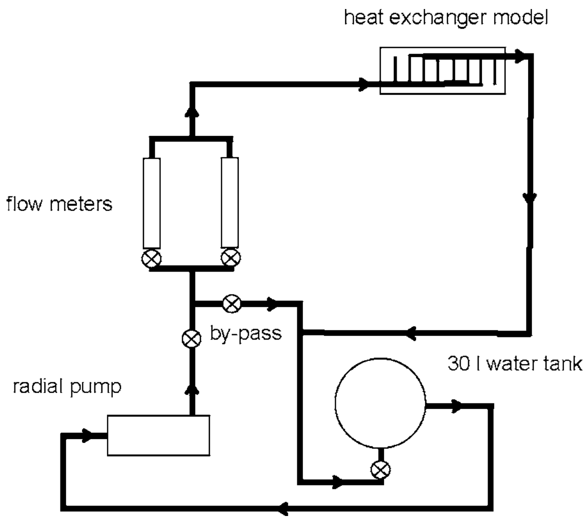

Fig. 1 Hydraulic loop

with changes in the duct diameter.

A full-scale heat exchanger model is made with aluminum and glass, this latter material permitting an easy optical access inside the central part of the tubes (Fig. 3). The heat exchanger consists of, following the flow direction: an inlet duct; an inlet collector feeding six parallel glass tubes, each one with a length of 44 mm; an outlet collector; and an outlet duct. The ducts and collectors are 8 mm dia, whereas the inside diameter of the tubes is 4 mm. The six parallel tubes and the inlet and outlet ducts are in the same plane, but the inlet collector is forming an angle of 25 deg with the parallel tubes plane, whereas the outlet collector is forming an angle of 155 deg with it. The exit of the inlet duct is located in front of tube number 2 and the entry of the outlet duct is in front of tube number 5. A stand-alone tube (on the right side of Fig. 3) with the same dimensions is placed on the model frame and can be fed by the water circuit, allowing the validation of the measurement technique on a well-known flow established inside a rectilinear channel. An additional tube (on the left of Fig. 3) contains a calibration target immersed in water for the measurement of the camera magnification.

2.3 Particle Image Velocimetry Apparatus

2.3.1 Laser Emission Device and Camera. Light emission is achieved with a laser YAG Quantel Twins Ultra, consisting of two sources emitting a 532 nm light flash with an energy of 30 mJ by pulse. Each pulse is 6 ns long. A cylindrical lens placed at the head emission end creates a light plane, which is directed toward the region of measurement by the means of a plane mirror. The image recording system consists of an 8-bit camera with 768 $\times$484 pixels, its focal depth is 25 mm. The image magnification

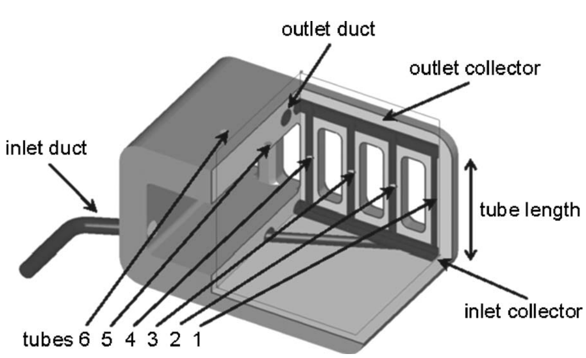

Fig. 2 View of the new heat exchanger model

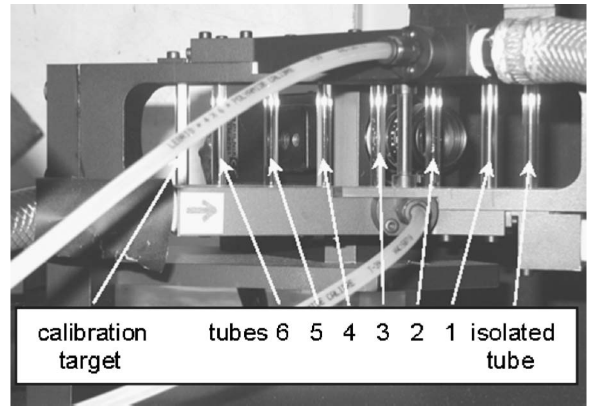

Fig. 3 Heat exchanger model

is 2.4. A Quantel DPS 01 box achieves the synchronization between laser emission and camera recording by the variation of the lag between two pulses. The laser emission head and the camera are placed on a one-axis traversing system to successively explore the flow inside each of the six tubes (Fig. 4). The axial translation accuracy is 1 μm. The laser sheet thickness is 0.25 mm and passes through the tube diameter without deviation along the tube height, forming an angle of 45 deg with the tube's alignment axis.

2.3.2 Optical Flow With Dynamical Programming. The method used for particle image displacement calculation is the optical flow using dynamical programming [18,19]. It is based on the minimization of the Minkowski L^p norm between two successive images. A division of the image in smaller and smaller slices allows the calculation of a displacement field by orthogonal iterations. The advantage of this method over other PIV methods is its ability to provide a high density field of one vector calculated by pixel, with high accuracy in the regions of strong gradient. Measurements are conducted with a mean ten pixel particle displacement between successive images. Thus, the time delay between two flashes is adjusted for the velocity inside the tube, and is varied from 84 μs to 422 μs. With this set of parameters, the measurement accuracy is 1/32 pixel, which corresponds to a relative velocity accuracy of 0.31%.

2.3.3 Image Filtering. A simple image-filtering method was developed in the course of this work and is compared to classical image-filtering techniques [20]. During the experiment setting, particular attention is devoted to laser light positioning and to the suppression of all the undesirable light reflections. However, some reflections remain in the recorded images and can alter the PIV processing (Fig. 5(*a*)). In order to eliminate these optical noise sources, it seems easy to subtract from an image with flow, an image recorded without flow where only undesirable reflections are present. But such a reference image is impossible to get straightforward because of the presence of the tracers in the flow, which modifies the background scattered light. An alternative to that issue is addressed in the average of all the recorded images with tracer images, statistically equally distributed in the measurement field. That reference image retains the undesired reflections and is well known for image subtraction in PIV measurements [21]. But this process implies a background noise estimate altered by the average of the particle traces. In addition, the average is affected by the light source variation with time. The image filtering obtained with this method is given in Fig. 5(*b*). Another classical way to obtain a reference image is to erode the initial image, which removes any isolated cluster, followed by a dilatation of the gray level. As a result, the only remaining traces are light reflections. This image can be used to filter the initial image, as it is presented in Fig. 5(*c*). To get rid of the light variation between the two sources and with time, an original and very simple method

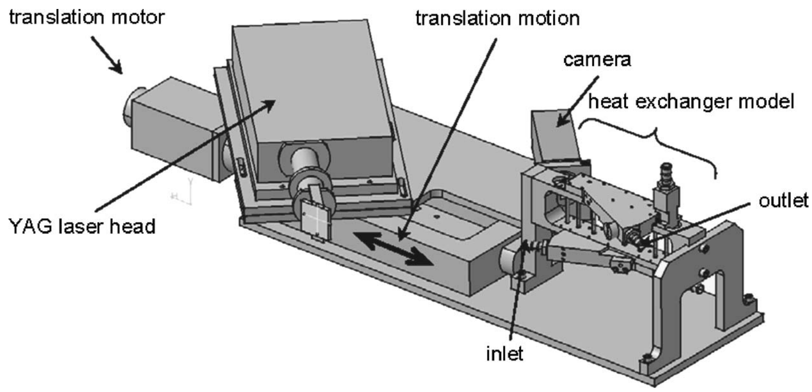

Fig. 4 Laser emission head and its translation system

has been implemented, which is compared to the previous ones. We have chosen to subtract to each image number n, the image recorded with the following flash coming from the same source, that is to say image number $n+2$ (Fig. 5(*d*)). It is worth noticing that almost no tracer identified on the rough image is rejected by this operation. The filtering residual can be estimated with the autocorrelation of the images. The zero correlation peak is identified on the images with any of the three filtering methods (Figs. 6(*b*)–6(*d*)), while the same peak is mixed with noise if no correction is applied (Fig. 6(*a*)). The cross-correlation of two successive images, without and with filtering, is given in Fig. 7. A correlation peak in zero is remaining with the method based on the erosion-dilatation (Fig. 7(*c*)). It is worth noting that, with the filtering by the subtraction of image n and $n+2$, as for the filtering with an averaged image, there is no residual zero displacement correlation peak, the only peak identified corresponds to the mean displacement of ten pixels. Figure 8 quantifies the improvement obtained by this processing with the histogram of the x average for the rough and filtered images (on the left) and with the cut of the cross-correlation at $\Delta y=0$ (on the right). One can observe the secondary peak at $\Delta x=0$ for the cross-correlation of the rough image, which vanishes completely on the filtered images. The only noticeable difference between the two filterings is the remaining wall tube reflections (Fig. 8, on the left, circle), which for filtering with an averaged image, is higher by a factor 2 in comparison to the filtering by subtraction of image n and $n+2$. Finally, the method based on the filtering by subtraction of image n and $n+2$ is used for this study.

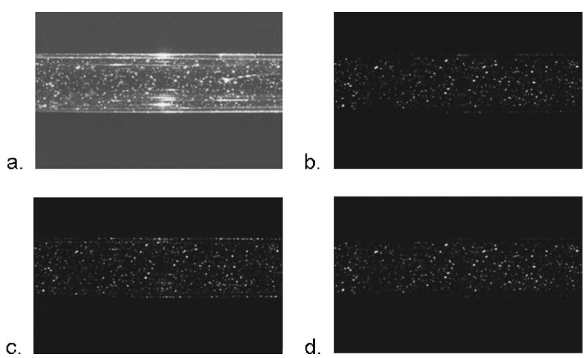

Fig. 5 Comparison between (*a*) a rough image, (*b*) an image with mean background noise subtraction, (*c*) with an eroded-dilated noise image subtraction, and (*d*) with subtraction of images *n* and *n*+2

2.3.4 Optical Deformations Correction. The optical path in the tube radial direction is modified by the presence of three media, air, glass, and water. The solution generally employed to reduce optical distortions with round tubes is to enclose the experimental setup within a rectangular water-filled box. In fact, an alternative solution was used for this study. The interfaces be-

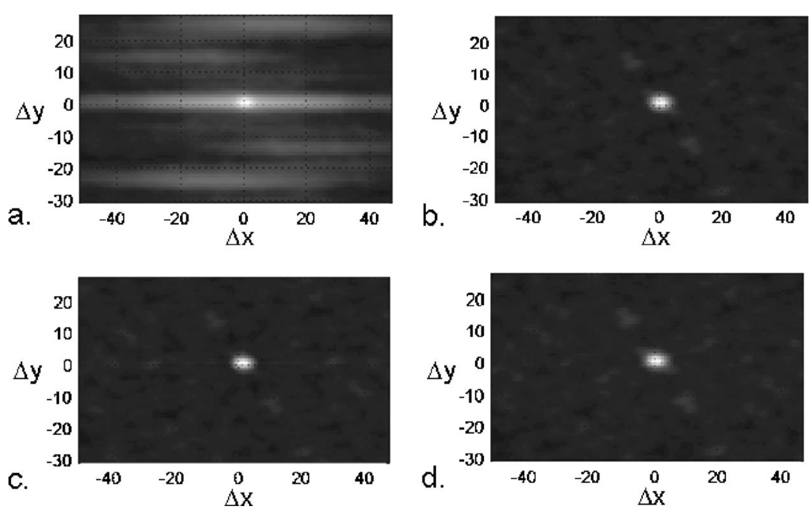

Fig. 6 Comparison between (*a*) the autocorrelation function of the rough image, (*b*) with mean background noise subtraction, (*c*) with an eroded-dilated noise image subtraction, and (*d*) with subtraction of images *n* and *n*+2

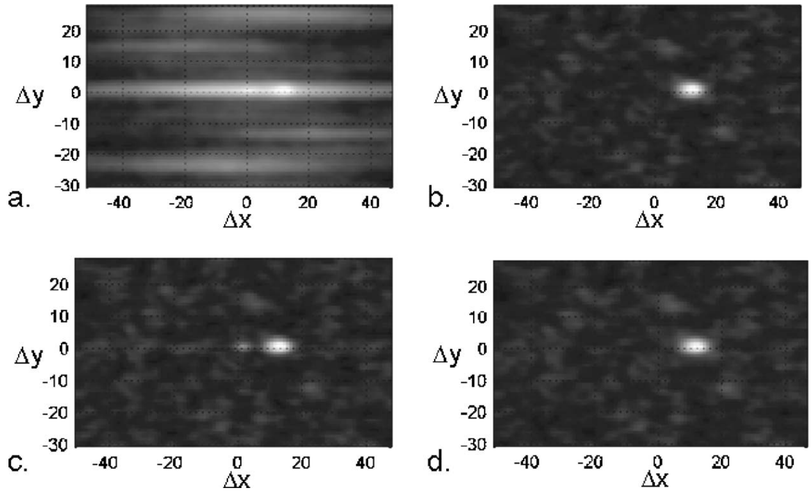

Fig. 7 Comparison between the cross-correlation function of (*a*) a couple of rough images, (*b*) with mean background noise subtraction, (*c*) with an eroded-dilated noise image subtraction, and (*d*) with subtraction of images *n* and *n*+2

tween air and glass, and between glass and water, generate light refractions and thus a deformation of the laser sheet image inside the tube and of the tracer image displacements (Fig. 9). A distance r inside the visualization plane will be observed as an apparent distance r_a inside the plane of the image of the camera, as a consequence of the angular deviations α_2, α_3, β_1, β_2.

The relationship between these two positions is obtained by solving

- Snell-Descartes equation for the interface between each medium

$$n_1 \sin \beta_1 = n_2 \sin \beta_2$$

$$n_2 \sin \alpha_2 = n_3 \sin \alpha_3$$

- The relationships of optical geometry provide the expressions for the angles α_2, α_3, β_1, β_2

$$\sin \alpha_2 = \frac{n_1}{n_2}\frac{r_a}{R_i}$$

$$\sin \alpha_3 = \frac{n_1}{n_3}\frac{r_a}{R_i}$$

$$\sin \beta_1 = \frac{r_a}{R_i + e}$$

$$\sin \beta_2 = \frac{n_1}{n_2}\frac{r_a}{R_i + e}$$

with the values of the refraction indices for air $n_1=1$, for glass $n_2=1.5$, for water $n_3=1.33$, and the internal tube radius $R_i=2$ mm and its thickness $e=1$ mm. The solution of this set of equations results in the apparent radial distance r_a as a function of the real radius r given by the expression plotted in Fig. 10

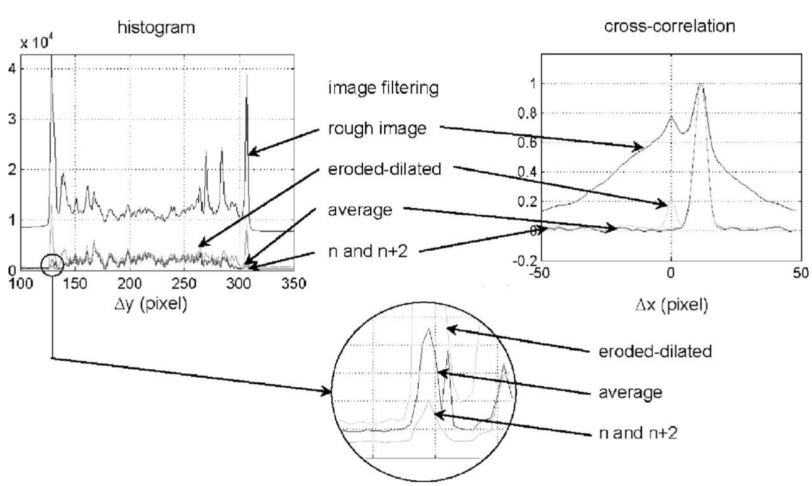

Fig. 8 Histogram of a rough image, with mean background noise subtraction and with subtraction of images *n* and *n*+2 (left) and cross-correlation at Δ*y* =0 for a couple of the same images (right)

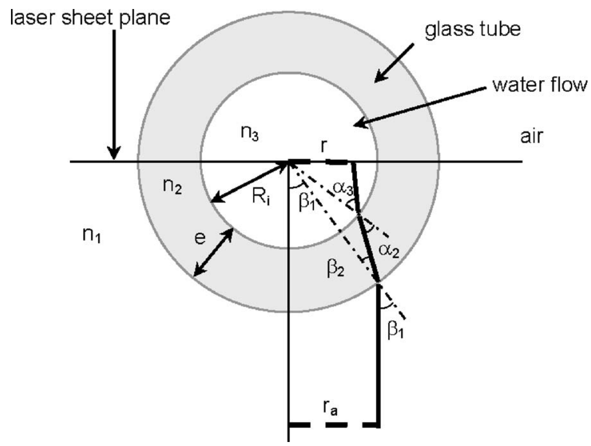

Fig. 9 Light path deformation caused by the different media

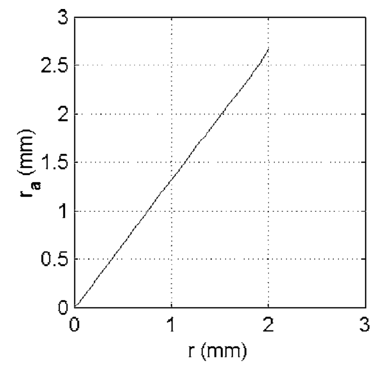

Fig. 10 Apparent radius function of the true radial position

$$r_a = r\frac{n_3}{n_1}\cos[\alpha_3 - (\beta_1 - \beta_2 + \alpha_2)]$$

This correction is taken into account for the radial positions for the measured displacements before velocity processing.

3 Results and Discussion

The flow inside the heat exchanger is investigated for flow rates between 3 l/min and 15 l/min, which correspond to inlet Reynolds numbers varying from 7960 up to 39,760. As the glass tubes are fixed in the aluminum frame and the camera positioning cannot be changed along the tube height, only the central half of the tubes length is explored in the plane of symmetry passing though the cylinder axes.

3.1 Error Analysis. We recall that PIV measurements are conducted with a mean ten pixel particle displacement between successive images. The time delay between two flashes is adjusted for the velocity inside the tube and is varied from 84 to 422 μs, according to the flow rate under consideration. With this set of parameters and the use of optical flow with dynamical programming for image displacement calculation, the measurement accuracy is 1/32 pixel, which corresponds to a relative velocity accuracy of 0.31%. The experimental results are obtained with the recording of 600 images providing 300 PIV fields for each tube. The average of these fields gives the mean velocity field inside each of the six heat exchanger tubes, with maximum statistical confidence accuracy on the mean velocity of 0.1m/s, corresponding to a maximum relative error of 2.5%. For the variances of the axial and radial velocity fluctuations and the shear stress of the axial-radial velocity fluctuations, the maximum statistical confidence accuracy is 0.015 m^2/s^2 corresponding to a maximum relative error of 5%.

3.2 Mean Flow. Mean velocity inside the measurement plane is obtained by PIV measurements. In order to analyze the flow behavior inside the six tubes, a grayscale map of the mean velocity field is provided for the central area of the tube, corresponding to the PIV camera field, with the same grayscale for each tube in Fig. 11, for the same inlet flow rate condition. The *x*-axis origin is located 11 mm downstream of the inlet collector-tube connection. We observe the axial evolution of the velocity profile. The distribution is strongly nonhomogeneous between the tubes, with a maximum velocity inside tube 2 and a minimum velocity inside tube 3. Figures 12 and 13 display the axial and radial velocity profiles inside the tubes for three axial positions of the investigated region. Inside tube 2, a strong axial velocity gradient is

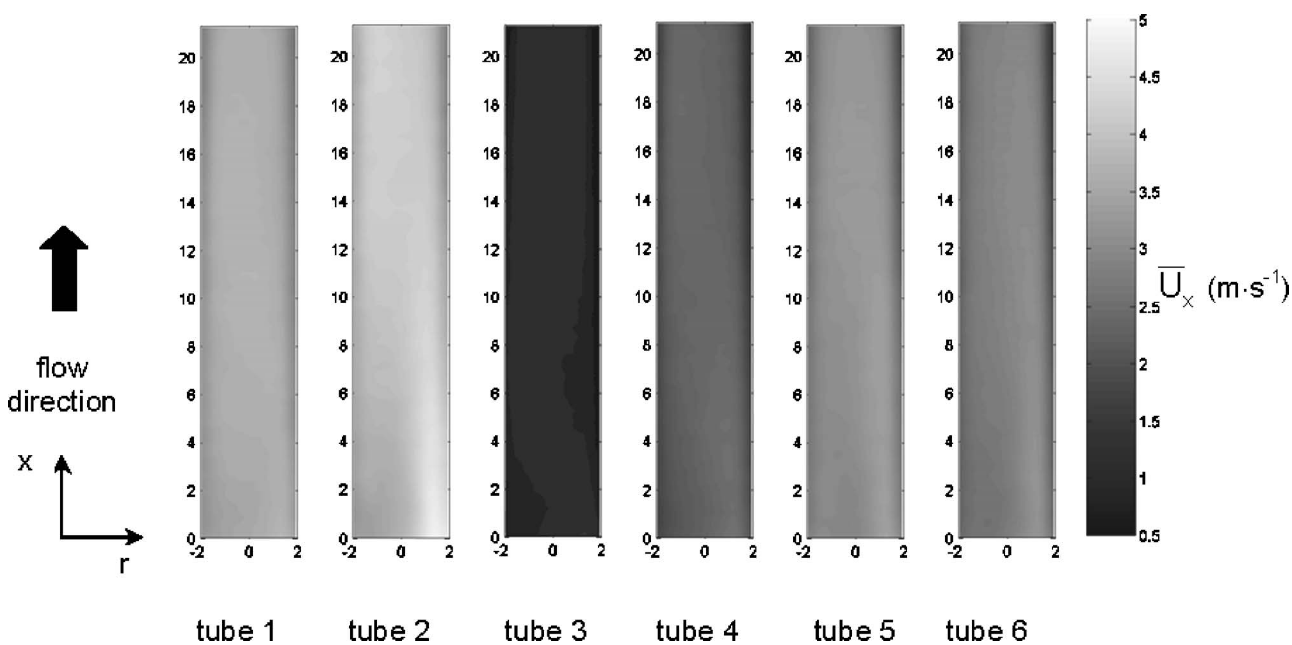

Fig. 11 Mean axial velocity distribution in the tubes for the inlet flow rate 12 l/min

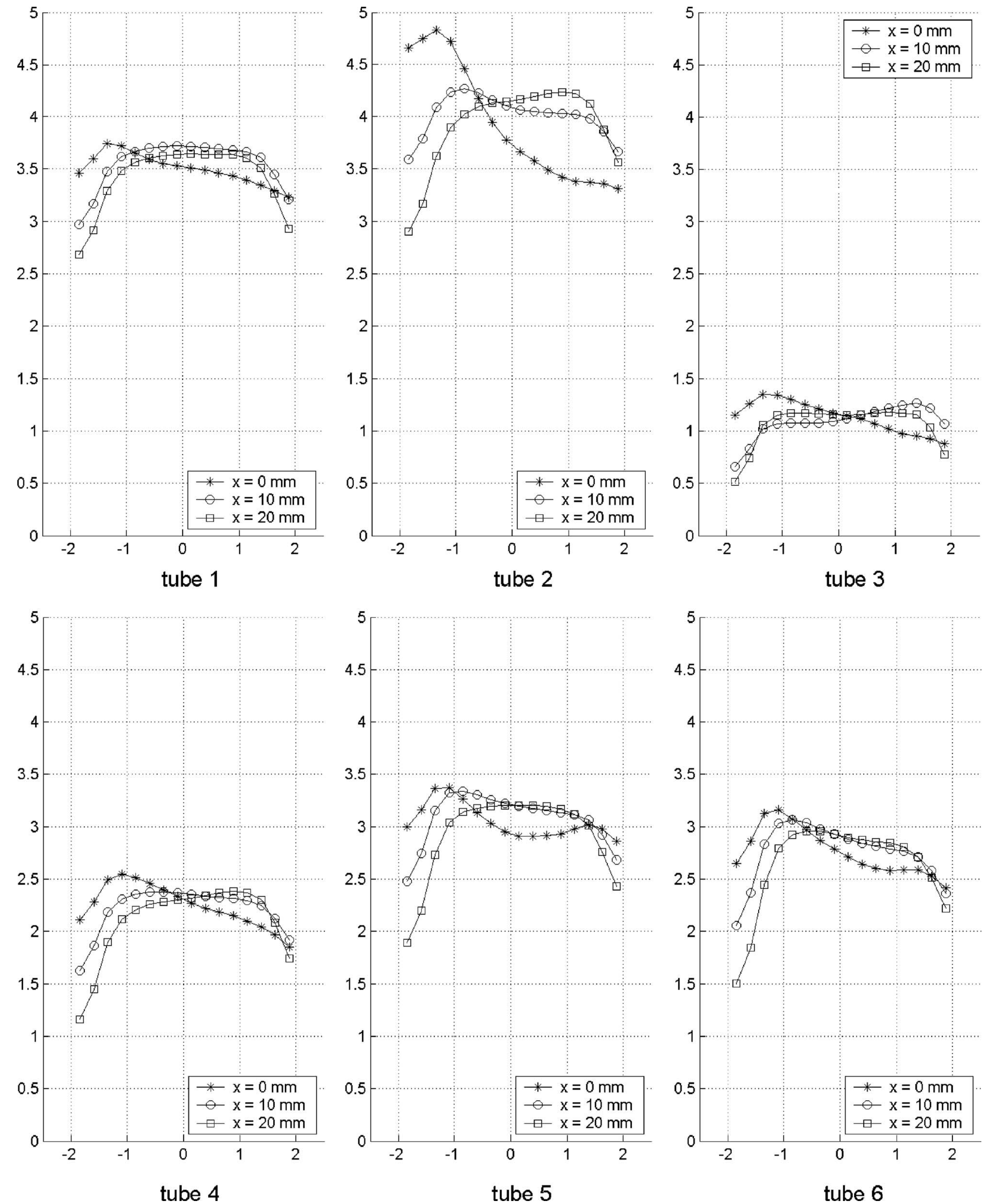

Fig. 12 Radial evolution of the axial velocity for three axial positions inside the tubes and for the inlet flow rate 12 l/min

present along a diameter for the first explored axial distance ($x=0$ mm). The velocity is smooth in the middle of the explored window ($x=10$ mm) and tends toward the inversion of the gradient for $x=20$ mm. This is evidence of the presence of a strongly nonestablished three-dimensional flow. The same behavior is found inside the other tubes. As the radial velocity and its gradient are small, the continuity equation yields to a strong gradient of the tangential velocity in the direction of the azimuth, which is not measured in the study. Tube 3 displays an axial velocity smaller a factor of 4 from tube 2. The radial gradient has the same shape at

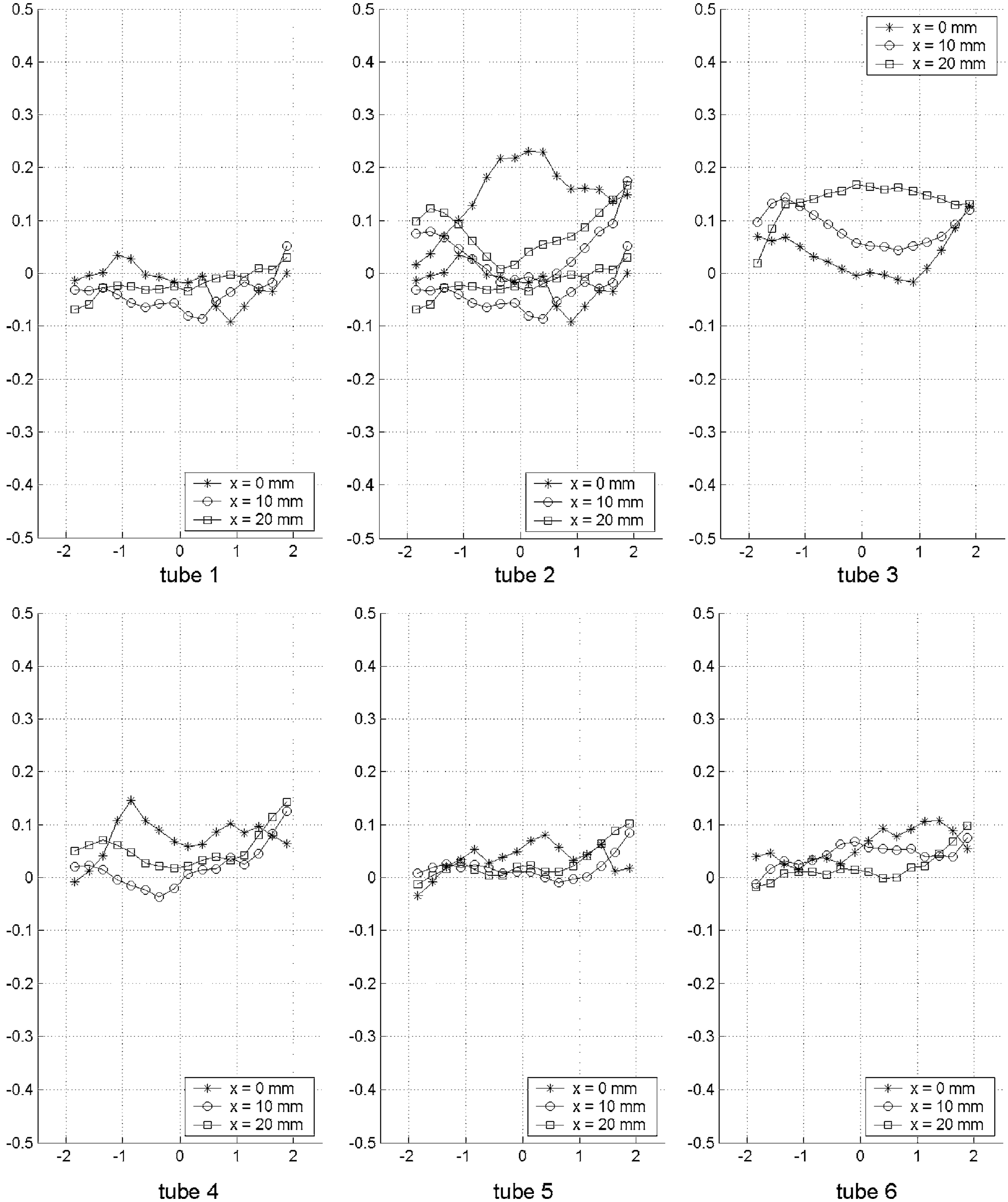

Fig. 13 Radial evolution of the radial velocity for three axial positions inside the tubes and for the inlet flow rate 12 l/min

$x=0$ mm, but is inversed for $x=10$ mm and shows an established profile for $x=20$ mm, which is consistent with the lower Reynolds number inside this tube. The radial velocity component and gradient remain low and are represented with a smaller scale in Fig. 13. The larger amplitude is found in tube 2 where the axial velocity is a maximum value. The heat transfer coefficient is proportional to the axial velocity gradient near the wall. As the axial velocity is zero on the wall, although it is not measured for this particular position, the greater the velocity inside a tube is, the larger the velocity gradient. The larger heat transfer between the fluid and the exchanger is obtained for tube 2. We observe on the axial velocity (Fig. 12) that the heat transfer is asymmetric inside each tube in the first half of the length and tends to a uniform distribution when the flow reaches an established velocity profile.

3.3 Velocity Distribution Between Tubes. The velocity is

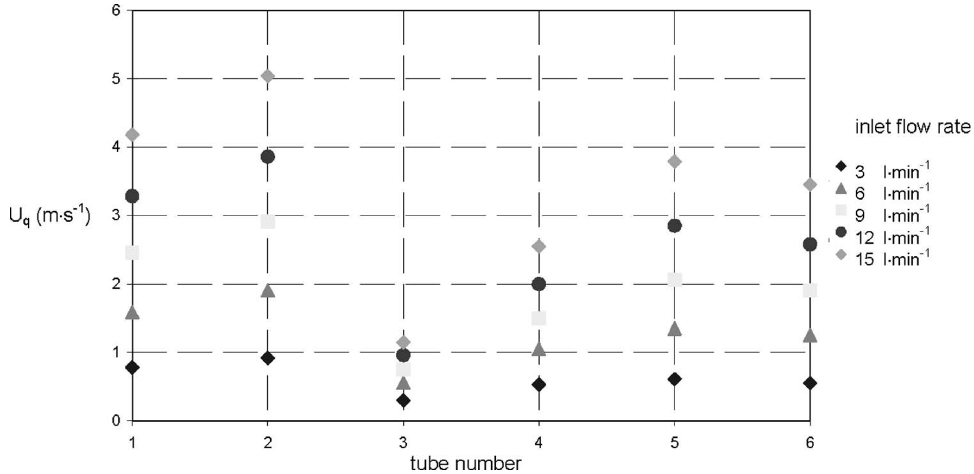

Fig. 14 Averaged reference velocity U_q distribution inside the tubes for five inlet flow rates

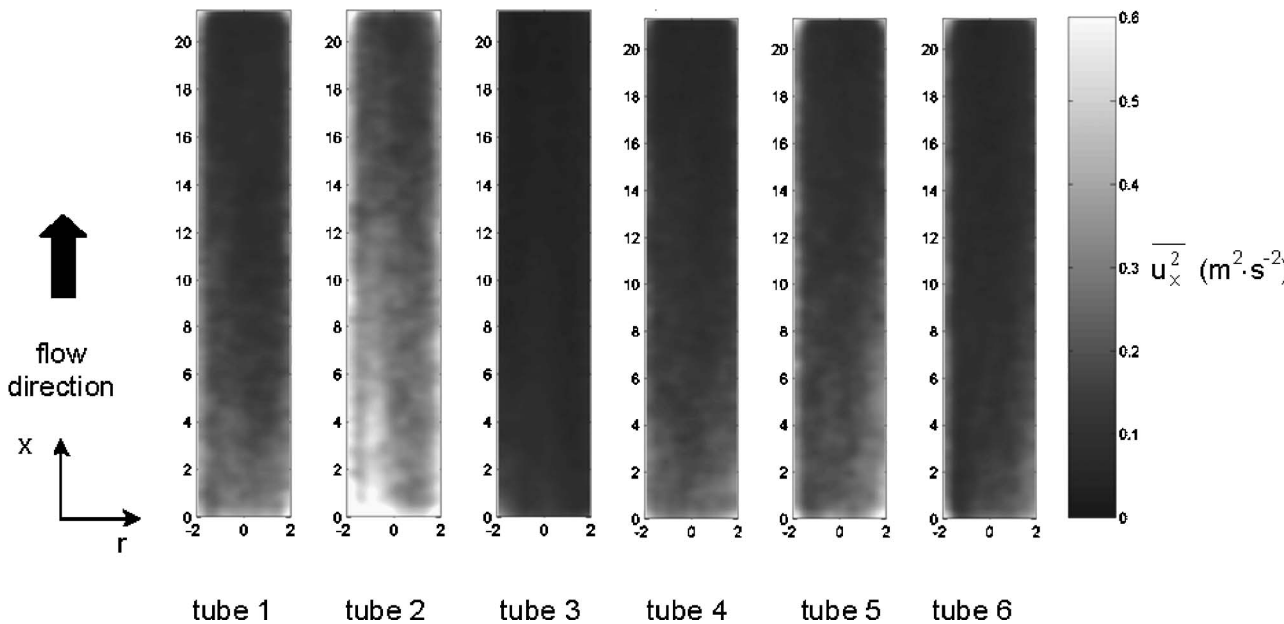

Fig. 15 Variance of the axial velocity fluctuations for the inlet flow rate 12 l/min

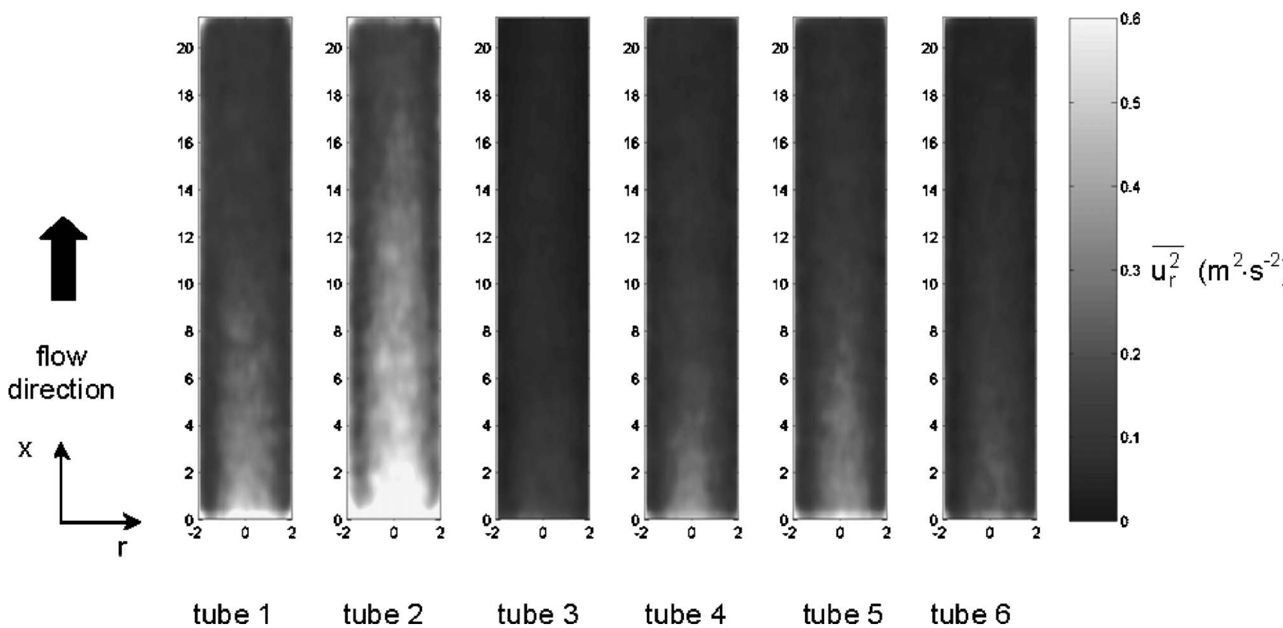

Fig. 16 Variance of the radial velocity fluctuations for the inlet flow rate 12 l/min

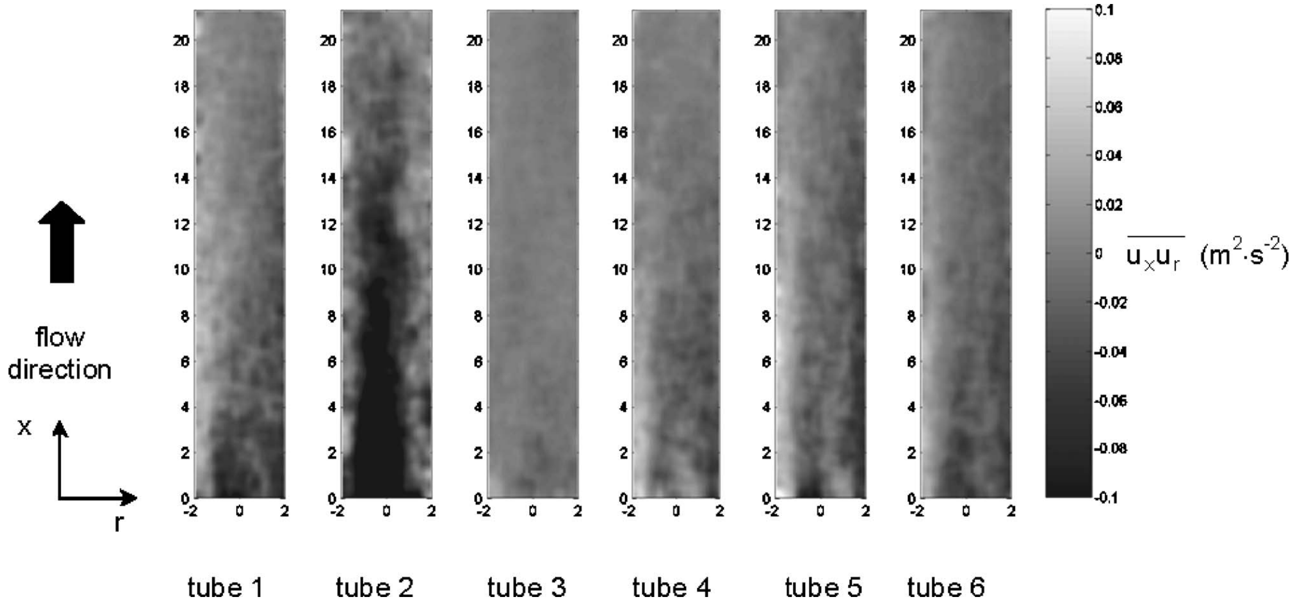

Fig. 17 Shear stress of the axial-radial velocity fluctuations for the inlet flow rate 12 l/min

averaged in the radial and axial directions and the distribution of the reference velocity U_q between the six tubes of the heat exchanger is displayed in Fig. 14, for five inlet flow rates varying from 3 l/min to 15 l/min. It has been checked that this reference velocity U_q is not far from the flow velocity through each one of the tubes by comparing the inlet flow rate measured with the flow meters to the integration of the measured velocities along the six tubes. For every inlet flow rate, the velocity distribution along the tubes shows a minimum value for tube 3 and a maximum value for tube 2, with a second local maximum value for tube 5. In fact, a careful examination of the heat exchanger geometry proves that tube 2 is in front of the junction between the inlet collector and the inlet duct and tube 5 is in front of the junction between the outlet collector and the outlet duct, which makes a traversing flow easier. This must be the reason why higher axial velocities are found inside these tubes for any flow rate.

3.4 Turbulent Flow. The statistical convergence of the second-order moments of velocity fluctuations is obtained with an estimated accuracy of 0.05 m^2/s^2 or a relative error of 0.3%. The variance of the axial velocity fluctuations (Fig. 15) shows a maximum intensity in the beginning of the investigation region and in the wall neighborhood of tube 2, which is the channel with the maximum flow rate. Note the dissymmetry of the variance of axial fluctuations with higher levels in the left part of the tube. That is the evidence of a recirculating region, which is present after the collector-tube connection and which spreads in the first third of tube 2. The turbulence is lower in the other tubes, especially inside tube 3, where the mean velocity is the lowest. Similar comments can be made for the variance of the radial velocity fluctuations (Fig. 16). The turbulence feature for the radial component is more symmetrical inside tube 2 than it is for the axial component. Figure 17 presents the axial-radial shear with higher amplitude and dissymmetry for tube 2. The large central negative region is typical of the recirculation coming from the connection between the inlet collector and tube 2. This is the evidence that the flow is highly anisotropic inside this tube.

4 Conclusion

The flow inside a heat exchanger, which is a component developed for cooling a high-current protons linear accelerator, has been investigated experimentally. A full-scale water model has been built for the study, and a PIV system has been implemented on the setup. The noise light refraction and displacement distortions inside the tubes have been corrected. Regarding the fluid dynamics inside the heat exchanger, the study focused on velocity distribution between each one of the small tubes. It is found, for the range of investigated inlet Reynolds numbers, that velocity distribution among the tubes does not depend on the flow rate. The global velocity field shows three-dimensional features. The velocity reaches a maximum value in tube 2 and a minimum value in tube 3, with a second relative maximum value in tube 5. For every inlet flow rate, the velocity ratio between tubes 2 and 3 is 4. The heat transfer coefficient is proportional to the velocity gradient near the wall, and it is asymmetric inside each tube in the first half of the length and tends to a uniform distribution when the flow is established. The larger velocity gradient inside tube 2 provides a larger heat transfer coefficient and a better heat transfer efficiency than the other tubes. The turbulent components measured show higher levels inside tube 2, which will be more efficient in terms of heat transfer.

Acknowledgment

The authors are indebted to A. Chaboche, A. Stephen, and L. Vatrinet, for building the facility, and to V. Bourdin and S. Rieublanc for the improvements brought to the hydraulic loop. They would like to thank D. Rougier, J. Bissiriex, and J. P. Baronick for the conception of the heat exchanger model.

References

[1] Idel'cik, I. E., 1986, "Memento des Pertes de Charges" (French translation from Russian) Eyrolles, Paris.
[2] Pedley, T. J., Schroter, R. C., and Sudlow, M. F., 1971, "Flow and Pressure Drop in Systems of Repeatedly Branching Tubes," J. Fluid Mech., **46**(2), pp. 365–383.
[3] Pedley, T. J., 1977, "Pulmonary Fluid Dynamics," Annu. Rev. Fluid Mech., **9**, pp. 229–274.
[4] Alharbi, A. Y., Pence, D. V., and Cullion, R. N., 2003, "Fluid Flow Through Microscale Fractal-Like Branching Channel Networks," ASME J. Fluids Eng., **125**, pp. 1051–1057.
[5] Haselton, F. R., and Scherer, P. W., 1982, "Flow Visualization of Steady Streaming in Oscillatory Flow Through a Bifurcating Tube," J. Fluid Mech., **123**, pp. 315–333.
[6] Manga, M., 1996, "Dynamics of Drops in Branched Tubes," J. Fluid Mech., **315**, pp. 105–117.
[7] Comer, J. K., Kleinstreuer, C., and Zhang, Z., 2001, "Flow Structures and Particle Deposition Patterns in Double-Bifurcation Airway Models. Part 1: Air Flow Fields," J. Fluid Mech., **435**, pp. 25–54.
[8] Zhang, Z., Kleinstreuer, C., and Kim, C. S., 2002, "Gas-Solid Two-Phase Flow

in a Triple Bifurcation Lung Airway Model," Int. J. Multiphase Flow, **28**, pp. 1021–1046.
[9] Corieri, P., 1994, "Experimental and Numerical Investigation of Flows in Bifurcations Within the Lung Airways," Ph.D. thesis, Université Libre de Bruxelles.
[10] Ramuzat, A., and Riethmuller, M. L., 2002, "Étude Expérimentale des Écoulements Oscillatoires dans un Modèle de Bifurcations Multiples Tridimensionnel," 8ème Congrès Francophone de Vélocimétrie Laser, Orsay (France), Sept. 17–20, pp. 125–130.
[11] Ramuzat, A., 2002, "Techniques de Mesures Non-invasives Appliquées aux Écoulements Biologiques: Étude des Bifurcations Pulmonaires Successives," Ph.D. thesis, von Karman Institute for Fluid Dynamics and Université Paris XII Val de Marne.
[12] Theunissen, R., Corieri, P., and Riethmuller, M. L., 2004, "Application de la PTV à la Modélisation d'Écoulements d'Aérosols dans les Voies Aériennes Pulmonaires," 9ème Congrès Francophone de Vélocimétrie Laser, Brussels (Belgium), Sept. 14–17, pp. K.5.1–K.5.9.
[13] Ku, D. N., 1997, "Blood Flow in Arteries," Annu. Rev. Fluid Mech., **29**, pp. 399–434.
[14] Rieu, R., Pelissier, R., and Farahifar, D., 1989, "An Experimental Investigation of Flow Characteristics in Bifurcation Models," Eur. J. Mech. B/Fluids, **8**(1), pp. 73–101.
[15] Ethier, C. R., Prakash, S., Steinman, D. A., Leask, R. L., Couch, G. G., and Ojha, M., 2000, "Steady Flow Separation Patterns in a 45 Degree Junction," J. Fluid Mech., **411**, pp. 1–38.
[16] Kubilay, E., 1982, "Répartition du Débit et Pertes de Charge Singulières d'un Absorbeur Solaire Tubulaire," Ph.D. thesis, Université Pierre et Marie Curie, Paris VI.
[17] Nikolaidis, N. M., and Mathioulakis, D. S., 2002, "Axial and Secondary Flow Study in a 90 deg Bifurcation Under Pulsating Conditions Using PIV," ASME J. Fluids Eng., **124**, pp. 505–511.
[18] Quénot, G. M., 1992, "The Orthogonal Algorithm for Optical Flow Detection Using Dynamic Programming," Proc. IEEE, **III**, pp. 249–252.
[19] Quénot, G. M., Pakleza, J., and Kowalewski, T. A., 1998, "Particle Image Velocimetry With Optical Flow," Exp. Fluids, **25**(3), pp. 177–189.
[20] Faure, T. M., Lusseyran, F., Gougat, P., and Launay, F., 2004, "Exploration de l'Écoulement dans un Échangeur de Chaleur Tubulaire par Vélocimétrie par Images de Particules," 9ème Congrès Francophone de Vélocimétrie Laser, Brussels (Belgium), Sept. 14–17, pp. K.4.1–K.4.8.
[21] Rémy, D., and Buisine, D., 2005, "Caractérisation à l'Aide de la Tomographie et de la PIV d'une Structure Spirale Apparaissant dans une Cavité Rotor-Stator Aspirée," Actes du Colloque FLUVISU 11, June 7–9, Ecully (France).